

Numerical Simulation of The Top Side-Pouring Twin-Roll Casting of 6.5 wt.% Si Steel Process

Dongpo Xuan

University of Science and Technology Beijing

cheng zhou (✉ zhouc_107@126.com)

University of Science and Technology Beijing

You Zhou

University of Science and Technology Beijing

Tianliang Jiang

University of Science and Technology Beijing

Biji Zhu

University of Science and Technology Beijing

Wenhao Fan

University of Science and Technology Beijing

Yangguang Jia

Advanced Technology Generalization Institute of CNCC

Research Article

Keywords: Twin-roll casting, Numerical simulation, Microstructure 6.5 wt.% Si steel

Posted Date: May 13th, 2021

DOI: <https://doi.org/10.21203/rs.3.rs-505124/v1>

License:  This work is licensed under a Creative Commons Attribution 4.0 International License.

[Read Full License](#)

Version of Record: A version of this preprint was published at The International Journal of Advanced Manufacturing Technology on December 9th, 2021. See the published version at <https://doi.org/10.1007/s00170-021-07973-9>.

Abstract

Using the commercial finite element software ProCAST to predict the temperature field, the flow field, the turbulent kinetic energy, and melt-pool outlet temperature of the top side-pouring twin-roll casting (TSTRC) of 6.5 wt.% Si steel process, and the cellular automaton–finite element (CA-FE) method was used to simulate the melt-pool outlet microstructure. The effect of different process conditions on the TSTRC process was investigated through numerical simulation and a processing technic appropriate for the production of 6.5 wt.% Si steel was obtained. Meanwhile, the influence of violent stirring in the melt-pool on the microstructure under different process conditions was evaluated. It was found that vigorous stirring in the melt-pool was conducive to formate the equiaxed crystal structure. Not only realized the near-final shape of the metal sheet, but also realized the near-final shape of the microstructure. Chose the proper process to experiment, and from comparing the simulation and the experiment, the simulation and experimental results were in good agreement, which verified the simulation's feasibility and accuracy.

1 Introduction

Twin-roll strip casting (TRC) is a near-net-shape process that combines casting and rolling techniques to cast and roll liquid metal into thin strips of 1 ~ 4 mm [1]. TRC has been proven to be a kind of high-efficiency and energy-saving technology [2]. Compared with traditional casting technology, TRC has attracted extensive interest because of the advantages of a shorter production process, lower investment cost, and operating cost. Besides, the mechanical properties of metal materials can be increased due to the rapid cooling in the casting process [3].

During the TRC process, the solidification, heat transfer, and possible plastic deformation of the metal are completed in a short time simultaneously. Additionally, the process parameters such as the pouring temperature, the casting speed, and the melt-pool height influence each other, making the TRC process very complicated to control. Therefore, the numerical simulation method can optimize the process parameters to reduce the cost and workload, which helps control the twin-roll casting process, product quality, and microstructure and properties.

Extensive research had been done on this technology, and many impressive results had been achieved. Tavares and Guthrie [4] systematically introduced the application of computational fluid dynamics in TRC, which provided tremendous help for later scholars in the study of TRC. Sahoo et al. [5] used FLUENT commercial software to model high-speed TRC and comprehensively verified the prediction results. Saitoh et al. [6] discussed the influence of various process parameters on the changing law of the solidified shell and analyzed the relationship between the kissing point and the process parameters. Hwang et al. [7] considered the fundamental transport phenomena of the TRC process and analyzed the flow field and temperature field in the melt-pool filling stage during the TRC process. Gupta and Sahai [8] developed a two-dimensional finite element model to research the influence of casting speed, heat transfer coefficient between melt-pool and roll, and molten steel superheat on strip thickness. Miao et al. [9] used a microsegregation model to probe the impact of the casting speed, the pouring temperature, and

the roll gap on the flow field and temperature field. Bae et al. [10] investigated the flow field and temperature distribution in the TRC process. They analyzed the influence of process parameters such as liquid level, casting speed, and nozzle size on the temperature distribution and velocity distribution in the melt-pool and its impact on the kissing point. Pei et al. [11] researched the temperature distribution in the melt-pool and the cooling rates under different casting conditions. He et al. [12] studied the relationship between cooling rate and microstructure evolution and mechanical properties under different casting methods. Their research believed that TRC has the potential to produce high-performance alloys. Zeng et al. [13] calculated the turbulent flow field for different steady-state casting points. They illustrated the influence of casting speed and roll gap width on the internal temperature field, flow field, and solidification structure. Li et al. [14] used thermal-fluid and thermal-mechanical finite element methods to simulate the temperature field, flow field, and stress field of the TRC process. The effects of casting speed and pouring temperature on temperature field, fluid flow field, and stress field during the process were analyzed. According to the study of Guan et al. [15], as the casting temperature increases, the solid fraction increases from the inlet to the outlet of the roll gap. The average grain size of the product increases with the casting temperature, and the plastic deformation along the rolling direction occurs. Sun et al. [16] studied the influence of vibration parameters on twin-roll strip vibration cast-rolling. They found that mechanical vibration introduced during the casting process can optimize grains and suppress segregation. The perturbation effect of vibration on the flow field of the molten pool can increase the nucleation rate. Zhao et al. [17] obtained the temperature distribution and the flow field in the casting-rolling zone through the finite element method. They found that the casting temperature increase caused the rise of the strip temperature at the exit. Rodrigues et al. [18] minimized the macrosegregation deviations in the strip and predicted an optimal strip quality in the TRC process. To increase the casting speed and expand the applicable range of alloys, Wang and Zhou [19] proposed the TSTRC, which revealed the regular heat transfer pattern between the metal and the roll surface TSTRC process. Zhang et al. [20] adopted the method of combining numerical simulation and water simulation experiments with studying the influence of the flow distribution system on the TSTRC process, which provided stable flow conditions for the TSTRC process. The melt flow, heat transfer characteristics, and stability control during the molding process were probed. Concurrently, the influence of the primary process conditions on the melt flow stability and heat transfer characteristics in the TSTRC process was clarified [21].

Predecessors' numerical simulation studies on the TRC process mainly focused on the flow, heat transfer, and solidification process in the melt-pool. The simulation results have particular guiding significance for subsequent research, but some problematic issues still need further study. In most numerical simulations, only a two-dimensional model was established to simulate the TRC process. However, the two-dimensional numerical simulation cannot accurately reflect the features of melt in the width direction. The majority of the numerical simulations treated the physical parameters of the material as constants for simulation. In fact, in the TRC process, different temperatures will inevitably cause changes in the material's mechanical behavior and physical parameters. If the simulation uses constant physical parameters, the results will have significant effects and even fail to reflect the actual situation of the

casting and rolling process. Simultaneously, the effect of stirring in the melt-pool on the solidification structure of the TRC process is rarely reported.

Regarding the issue above, the heat transfer, mass transfer, flow, and solidification processes were coupled, and a three-dimensional finite element model was established. Besides, the material thermophysical parameters that change with temperature were used for numerical simulation analysis. Based on the above conditions, the TSTRC process under different process parameters was simulated numerically. Meanwhile, a 2mm×2mm area was cut out at the melt-pool exit, and the microstructure was simulated by the CA-FE method.

2 Physical Model And Boundary Conditions

Based on the casting and rolling equipment in our laboratory, a three-dimensional model as shown in Fig. 1a and a simulation calculation area as shown in Fig. 1b was established, and the following basic assumptions were made:

1. The rolls are not deformable and rotate at a uniform speed.
2. The contact surface of the melt and the roll has no slippage.
3. The molten steel is regarded as an incompressible Newtonian fluid.
4. Heat losses by radiation are negligible.
5. Ignore the influence of natural convection caused by buoyancy.
6. The environmental temperature is assumed as 25°C.

2.1 Physical model description

Figure 2a shows the schematic diagram of the TSTRC. Figure 2b is the partially enlarged view of the melt-pool. "V" is the casting speed, "H" is the melt-pool height, "The kissing point" is the point where two solidified shells meet. The TSTRC process is described as follows: the molten metal with certain superheat is delivered uniformly through the delivery system at a constant flow rate to the lower roll surface. After a period of cooling of the lower roll, the interface will form a thin shell of solidified metal, and then the molten metal will flow into the melt-pool formed by two rolls and side dams. Due to the "pre-cooling" effect on the lower roll surface, the melt is easier to solidify and form the other solidified shell when contacting the upper roll's chilling surface. The two solidified metal shells have been meshed together before leaving the roll gap, and the solidified metal is rolled when it passes through the roll gap and becomes a strip.

2.2 Boundary conditions

$T = T_0$ (T_0 : inlet temperature), $u = u_0$, $v = v_0$, $w = 0$.

$v_{roll} = v_{out}$, the roll speed was equal to casting speed.

In this paper's simulation, the roll's material is 5CrMnMo die steel, the density is 7830 Kg/m³, and the thermal conductivity is 33 W/ m.°C, the specific heat capacity is 460 J/Kg. °C. The value range of the heat transfer coefficient between the metal and the roller is between 0.8×10⁴~2.0×10⁴ W/ m².°C [22], and the heat transfer coefficient in this paper is 1×10⁴ W/ m².°C.

Table 1
Casting parameters and physical properties of 6.5 wt.% Si steel.

Casting parameters	Values	Physical parameters	Values
Diameter of Upper roll/ Lower roll (m)	0.2/0.4	Liquidus temperature (°C)	1422
Roll gap (mm)	2	Solidus temperature (°C)	1382
The angle between rolls and horizontal line (°)	45	Latent heat of fusion (kJ/kg)	272
Pouring melt temperature (°C)	1437–1477	Liquid heat capacity (J/kg·°C)	784.3
Casting speed (m/s)	0.4–1.2	Solid heat capacity (J/kg·°C)	790
Melt pool height (mm)	25–45		

Table 1 shows the casting parameters and physical properties of 6.5 wt.% Si steel. In the numerical simulations, the parameters such as density, viscosity, enthalpy, and thermal conductivity are adjusted with temperature changes, as shown in Fig. 3, which may make the simulation more accurate, similar to the actual experiment.

3 Results And Discussion

3.1 Effect of pouring temperatures

The pouring temperature plays a predominant role in the TSTRC process. The simulation with a melt-pool height of 45 mm and the casting speed at 0.4 m/s was carried out, the initial pouring temperature varied from 1437 °C~1477 °C, and all other parameters were kept constant.

To better reflect the effect of the flow field on the temperature field and turbulent flow energy, the central symmetry plane of the melt-pool is intercepted in the three-dimensional results to study and analyze the effect of the stirring effect.

Figure 4a, b, c shows the melt-pool temperature and flow fields at different pouring temperatures. The arrow direction indicates the flow direction of the melt, and the length of the arrows represents the relative velocity value. As the pouring temperature increased, the melt-pool temperature was high and uneven. The solidus and liquidus position decreased, and the liquid phase area and the temperature gradient increased. This is because under other conditions unchanged, as the pouring temperature increases, the heat in the melt-pool increases, the cooling rate of the melt is slower, the solidified shell is thinner, and the

heat exchange effect is poor. It can be seen from the flow field in Fig. 4a, b, c, the melt rushes into the wedge-shaped zone at a certain speed, and space is sharply reduced, and the squeeze effect of the twin rolls works together, a part of the melt is forced to flow back, while the upstream melt is still flowing at its original speed. At the intersection of the two melts, the melt flow in the direction of least resistance, that is, towards the liquid surface. After reaching the liquid level, the melt disperses under the action of gravity. When entering the area affected by the roll speed, the rotating roll is driven forward to the roll gap so that the cycle repeats to form a vortex [23]. This forced convection has the benefit of improving the uniformity of temperature and composition [24]. The pouring temperature change did not significantly change the flow trend of the molten steel in the melt-pool. The vortex area inside the melt-pool did not change significantly, and the position of the vortex increased slightly with an increase in the pouring temperature. Because the temperature of the molten steel in the upper part of the melt-pool is relatively high, the viscosity of the molten steel changes less, and the temperature rise has little effect on the flow field in the melt-pool region.

As shown in Fig. 4d, e, f, the results showed that the solidified shell thickness decreased with the temperature change. Furthermore, it can be seen in Fig. 5c, the height of the kissing point was reduced from 21 mm to 10 mm. Generally speaking, as the pouring temperature increases, the superheat in the melt-pool increases, the heat of the melt in the melt-pool is larger. The rolls take away less heat, allowing the liquid pocket to move to the melt-pool outlet, decreasing the length and thickness of the solidified shell, which will reduce the heat exchange effect between the roll and the melt.

As shown in Fig. 5a, b, as the pouring temperature increased, the temperature increased at the melt-pool outlet, and the central temperature rose significantly. The results were consistent with the results obtained by Kim et al. [25]. The temperature difference between the surface and the center increased simultaneously. The temperature variation increased from 32 °C to 66 °C, the temperature at the centerline of the melt-pool outlet was distributed evenly across the width. When the pouring temperature is too high, the high-temperature area is more comprehensive. The viscosity in the upper part is low, and the central area is prone to incomplete solidification. It is easy to cause liquid leakage accidents, adversely affecting the continuity of the TSTRC process, and easy to oxidize the melt and the surface of the strip. Zhang et al. [26] also believe that high casting temperatures are likely to oxidize the melt and thin strips, suggesting that the pouring temperature should be as low as possible. However, suppose the pouring temperature is too low. It is possible to cause the rolling force to be excessive, which can cause the thin strip to crack and negatively affect the continuity in the production process. More severe cases can trigger a rolling accident. So, it is crucial to choose a suitable temperature in the pouring process.

Figure 4g, h, i shows the turbulent kinetic energy and flow field distribution in the melt-pool at different pouring temperatures. As the pouring temperature increased, the turbulent kinetic energy in the liquid and solid-liquid two-phase regions in the melt-pool increased. When the pouring temperature was 1437 °C, the turbulent kinetic energy of the melt-pool was primarily distributed in 200 ~ 500 cm²/s². The pouring temperature was 1457 °C, and 1477 °C, the turbulent kinetic energy in the melt-pool was distributed chiefly in 400 ~ 500 cm²/s². Due to the increase of the pouring temperature, the temperature in the melt-

pool increases, and the velocity in the flow field also slightly increases, the viscosity of the liquid phase region and the solid-liquid two-phase region in the melt-pool decreases, and the vortex increases, so that the turbulence intensity in the melt-pool slightly increases, and the stirring in the melt-pool is also somewhat more intense.

Figure 6 shows the microstructure and the grain size of the melt-pool exit at different pouring temperatures. The structure in Fig. 6a, b, c is an equiaxed crystal structure, and with the increase of casting temperature, the microstructure increases significantly. It can also be seen from the figure that the structure on the lower roll side is slightly larger than that on the upper roll side. This is caused by the difference in the contact time between the molten steel and rollers. The molten steel first contacts the surface of the lower roller. After the lower roller is pre-cooled, the superheat degree is reduced, so the solidification structure on the upper roll side is smaller, as shown in Fig. 9a, b, c, and Fig. 12a, b, c are also a similar result and reason. Figure 6d, e, f shows that the average grain size increases from $65\mu\text{m}$ to $125\mu\text{m}$. As the pouring temperature increases, the temperature in the melt-pool gradually increases. Higher temperatures cause dendrites to be re-melted, which is not conducive to the preservation of dendrites. Liu et al. [27] have reported that reverse flow exiting the TRC process can re-melt and break dendrite arms. Therefore, as the pouring temperature increases, the melt-pool nucleation rate decreases, and the grain size increases. Pirhayati and Aval [28] consider that a higher cooling rate will lead to fine grains. Wherefore the cooling rate of the melt is fast, and the undercooling is large, the liquid phase at the front of the solid-liquid interface is more comfortable to nucleate, thereby easily forming a fine equiaxed crystal structure. Moreover, Wei and Li [29] believe that enormous turbulent kinetic energy can promote equiaxed crystal structures. Because the melt-pool flow field is relatively turbulent, the stirring is violent. The turbulent kinetic energy in the melt-pool is also considerable, breaking some dendritic arms based on heterogeneous nucleation. Under this stirring action, the crystal nucleus forms on the surface of the roller can be washed down, and the crystal nucleus forms on the surface of the roll can be swept down in the melt-pool under the action of the rotation and squeezing of the double rolls. At lower pouring temperature, the solidified shell in the melt-pool is thicker so that the heat transfer effect between the melt and the rolls is sufficient. The sizeable cooling rate and powerful stirring effect promote equiaxed crystals at the exit of the melt-pool.

3.2 Effect of casting speeds

Casting speed is closely related to the process of the TSTRC, as it is directly proportional to productivity. In the simulation process, the initial pouring temperature of $1457\text{ }^\circ\text{C}$ and the melt-pool height of 45 mm maintained at a constant speed of $0.4\text{ m/s} \sim 1.2\text{ m/s}$, and other parameters unchanged.

Figure 7a, b, c shows that the change in temperature field and flow field within the melt-pool is achieved at various speeds from 0.4 m/s to 1.2 m/s . As the casting speed increased, the melt-pool temperature distribution changed considerably, and the temperature distribution became uneven. The melt-pool temperature generally rose, the region of the liquid phase significantly increased with an increase in casting speed. The position of the solidus and liquidus decreased obviously with the rise in the casting

speed. The rise in casting speed did not have a critical impact on improving the molten steel flow pattern in the melt-pool, and there was no apparent shift in the flow field vortex and location. With the increase of the casting speed, the vortex range increased, the flow velocity in the melt-pool increased, and the flow field was more turbulent. Since the faster the casting speed, the shorter the residence time of the molten steel in the melt-pool, and the faster the cooling time of the double rollers to the melt, the less sufficient heat exchange between the molten steel and the rolls in the melt-pool. As the casting speed increases, the linear speed of the roll speed also increases accordingly. In the sense of a constant roll gap, while keeping the melt-pool size unchanged, the inlet velocity of the melt increases simultaneously. The combined effect of the two causes the convection velocity of the melt in the melt-pool to increase, and the reflux is also more intense, increasing the size and velocity of the vortex area.

As shown in the solidification field in Fig. 7d, e, f, and the solidified shell thickness as shown in Fig. 8c, the kissing point's height decreased from 16 mm to 3 mm with the casting speed increased. As the casting speed increases, the cooling time of the melt on the roll surface will decrease, which will cause the liquid pocket to move toward the outlet of the melt-pool, thereby resulting in a reduction in the length of the solidification section.

As shown in Fig. 8a, b, when the casting speed rose, the temperature and the temperature fluctuation at the exit of the melt-pool increased. The temperature differential between the surface and the center rose from 50 °C to 83 °C. Significant temperature differences may increase the thermal stress of thin strips and increase the likelihood of surface cracking. The casting speed determines the residence time of the melt in the melt-pool and determines the cooling time of the melt. The casting speed increase makes the melt stay in the melt-pool shorter, resulting in a shorter cooling time of the melt, the heat loss of the melt decreases, which may cause the melt to flow out of the roll gap before it has cooled. Lee et al. [30] also consider that as the casting speed increases, the melt's heat loss through the cooling rolls decreases. Suppose the casting speed is faster than 1.2 m/s, most metal in the melt-pool is in the liquid and solid-liquid two-phase region, causing an incomplete solidification of the melt at the melt-pool outlet, then affect the quality of the thin strip, and may cause strip breakage or breakout accidents. When the casting speed is too slow, the kissing point is far from the melt-pool outlet, the temperature of the outlet region decreases, the solidifying region increases, and the rolling force increases may cause a production accident of the rolling card. Therefore, it is necessary to choose the right casting speed.

Figure 7g, h, i shows the turbulent kinetic energy in the melt-pool at different casting speeds. As the casting speed increased, the turbulent kinetic energy in the liquid and solid-liquid two-phase regions in the melt-pool increased, the stirring was intense. When the rolling speed was 0.4 m/s, the turbulent kinetic energy in the melt-pool was mainly distributed in 400 ~ 500 cm^2/s^2 . When the rolling speed was 0.8 m/s, the turbulent kinetic energy in the melt-pool was mainly distributed in 400 ~ 600 cm^2/s^2 . When the casting speed was 1.2 m/s, the melt-pool turbulent flow energy was primarily distributed in 500 ~ 600 cm^2/s^2 . As the casting speed increased, the flow velocity and vortex of the molten steel in the melt-pool rose. Simultaneously, to maintain the dynamic balance of the melt-pool height, the inlet speed of the melt-pool needs to be increased, which directly leads to a significant increase in turbulent flow energy.

Figure 9 shows the microstructure and grain size at the exit of the melt-pool at different casting speeds. With the increase of the casting speed, the equiaxed crystal structure in the melt-pool outlet gradually increased, and the average grain size increased from 80 μm to 180 μm . Due to the increase of casting speed, the residence time of the molten steel in the melt-pool reduces, the convective heat exchange with the rolls is insufficient, resulting in a rise in the temperature in the melt-pool and a decrease of undercooling, and the solid-liquid two-phase region in the melt-pool decreases, resulting in the reduction of the nucleation rate. The turbulent kinetic energy inside the melt-pool is more significant when the casting speed is high, and the stirring is intense, the crystal nuclei on the roll surface can be washed down, some dendrite arms can be broken. Nevertheless, due to the high temperature in the melt-pool, it is easy to melt the crystal nucleus and the dendrite arms, leaving only a tiny part in the melt-pool as a base for heterogeneous nucleation. Therefore, the nucleation rate in the melt-pool decreases, and the microstructure at the melt-pool outlet increases.

3.3 Effect of melt-pool heights

The change in the melt-pool height directly affects the temperature field and the flow field in the melt-pool and then affects the quality of the thin strip. In the simulation, the initial casting temperature was 1457°C, the casting speed was 0.4 m/s, the height of the melt-pool varied from 25 mm to 45 mm, and all other parameters remained constant.

Figure 10a, b, c indicates the melt-pool temperature and flow field distribution at various melt-pool heights. With the melt-pool height increased, the melt-pool temperature gradually decreased. The liquid phase region ratio in the melt-pool decreased, the solid phase region ratio and the solid-liquid two-phase region increased, and solidus and liquidus positions moved up obviously. When the melt-pool height increased, the vortex range and the melt-pool volume increased accordingly, and the vortex morphology was roughly similar. As the melt-pool height increases, the contact length between the melt and the rolls increases, enhancing the heat exchange effect between the melt and the rolls, so the cooling rate of the melt is fast, and the temperature field distribution in the melt-pool is more evenly. Besides, the vortex has sufficient reflux space, and the residence time increases so that the vortex in the melt-pool develops more fully. The full development of the vortex leads to a more uniform temperature distribution of the molten steel in the melt-pool. Also, it makes the temperature distribution in the width direction more uniform.

As shown in Fig. 10d, e, f, and Fig. 11c, as the melt-pool height increased, the kissing point's height increased from 4 mm to 16 mm, and the thickness of the solidified shell increased. The melt pool height determines the continuous contact time of the melt with the two rolls and therefore determines the cooling time. When the stable melt-pool is less than 25 mm, the contact length between the melt and the upper roll is short. Most of the melt is in the two-phase region, and the solidified layer is thin. Until leaving the roll gap, the solidified layers on the upper and lower roll sides do not have enough thickness to complete the welding and cannot form the thin strip if the melt does not overflow the melt-pool. As the melt-pool height increases, the contact length between the melt and the upper roll increases. So the

solidified layer becomes thicker, and the two solidified layers will be welded together before leaving the roll gap, the quality of the thin strip will be better.

Figure 11a, b is the temperature from the surface to the center at the melt-pool outlet. The temperature differential between the surface and the center of the melt-pool outlet decreased from 105 °C to 58 °C as the melt-pool height increased. As the melt-pool height increased, the temperature fluctuation of the centerline decreased, and the relative temperature distribution at the center of the melt-pool outlet became uniformly. The increase in the melt-pool height increases the contact length between the upper roll side melt and the roll surface and enhances the double-sided cooling effect, thereby increasing the thickness of the solidified shell. The increase in the solidified shell thickness will enhance the heat exchange effect between the melt and the roll. Therefore, the increase in the melt-pool height enhances the heat exchange effect while increasing the solidified shell thickness. Therefore, when the melt does not overflow the melt-pool, the higher the melt-pool height, the better the surface quality of the strip.

Figure 10g, h, i shows the turbulent kinetic energy at different heights of the melt-pool. As the melt-pool height increased, the turbulent kinetic energy in the liquid and solid-liquid two-phase regions in the melt-pool decreased. When the melt-pool height was 25 mm, the turbulent kinetic energy of the liquid and solid-liquid two-phase regions in the melt-pool was relatively large, and the part with considerable turbulent kinetic energy distributed in 400 ~ 600 cm²/s². When the melt-pool height increased to 35 mm and 45 mm, the turbulent kinetic energy in the melt-pool was reduced, and the larger part of the turbulent kinetic energy was distributed in 200 ~ 500 cm²/s². Mainly because of the change in the melt-pool volume under the constant casting speed. The lower the melt-pool height, the smaller the melt-pool volume.

Figure 12 shows the distribution of the microstructure and the grain size at different melt-pool heights. It can be seen from Fig. 11a, b, c that the solidification structure at different heights of the melt-pool is a uniform equiaxed crystal structure. As the melt-pool height increased, the melt-pool microstructure gradually decreased, and the average grain size decreased from 115 μm to 80 μm. Since the lower the melt-pool height, the worse the heat exchange effect between the molten steel and the roll's surface, resulting in a higher temperature in the melt-pool, a smaller solid-liquid two-phase region, a broader temperature gradient. Moreover, there are fewer crystal nuclei in the melt-pool, so when the melt-pool height is lower, it is easy to form a sizeable equiaxed crystal structure. When the melt-pool height is higher, the contact length between the melt and the roll is longer, the double-sided cooling effect is excellent, and the cooling rate is fast, so the undercooling and the nucleation rate is large. The solid-liquid two-phase region increases and the temperature gradient decreases, and the liquid phase at the front of the solid-liquid interface is more comfortable to nucleate. Santos et al. [31] believe that the broader solid-liquid two-phase region is conducive to increasing nucleation rate. Furthermore, because more crystal nuclei in the melt-pool, the crystal nuclei contact each other under a lower temperature gradient and stop growing. The formation at the melt-pool exit is relatively uniform tiny equiaxed crystals.

4 Experimental Verification

From the above simulation results, it could be seen that lower melt-pool height, too high or too low pouring temperature, and casting speed had a terrible influence on the quality of thin strips and the continuity of production. If the pouring temperature is too high, the casting speed is too fast, or the melt-pool height is too low, it is easy to cause the thin strip to break, as shown in Fig. 13a. On the contrary, the stuck sample is shown in Fig. 13b is likely to cause rolling accidents, which is consistent with the prediction of the previous results. Therefore, it is imperative to select appropriate process parameters for experimentation. So, in the process of producing 6.5 wt.% Si steel by TSTRC, a melt-pool height of 45 mm, a pouring temperature of 1457 °C, and a casting speed of 0.4 m/s were selected to obtain the 6.5 wt.% Si steel strip.

Conducted several experiments in this process. The raw materials used in the experiment are pure silicon and pure industrial iron with a purity of 99.99%. Put clean, pure iron and pure silicon into an induction heating furnace, and melt the raw materials under argon gas protection. When the molten steel is stirred evenly under electromagnetic action, use the AS852B infrared thermometer and disposable thermocouple to measure the molten metal's temperature and pour when the temperature of the molten metal stabilizes at 1457°C. When the molten metal flows into the roll surface with a roll speed of 0.4m/s, the automatic control system is triggered, and the molten pool is maintained at 45mm through the automatic control system, and then a thin strip is obtained. Use the AS852B infrared thermometer fixed on the bracket to measure the temperature on the centerline of the melt-pool outlet and the surface temperature of the melt-pool outlet, and transfer the data to the computer for record-keeping, the comparison between the melt-pool outlet temperature obtained through multiple experiments and measurements and the simulation results is shown in Fig. 14. It can be seen from the comparison in the figure that the simulation and the experiment show good consistency. To quantify the error between the experimental and numerical results, Root Mean Square Error (RMSE) [32] defined:

$$T_{RMSE} = \sqrt{\frac{1}{N} \sum_{i=1}^N (T_{exp} - T_{sim})^2}$$

In the formula, T_{exp} and T_{sim} are the outlet temperature values of the melt-pool obtained by experimental measurement and simulation calculation, respectively, and N is the number of test groups. According to the calculation of the equation, the T_{RMSE} at the centerline of the melt-pool is 0.188, and the T_{RMSE} at the exit surface of the melt-pool is 0.274. The results show that the simulation results have high accuracy.

Figure 15a shows the thin strip taken by the camera during the TSTRC experiment, and Fig. 15b shows the thin strip after cooling. The surface quality of the thin strip was superior, and the edges of the strip were flush. Figure 16 shows the microstructure distribution obtained at the melt-pool exit through simulation and experiment. The area of 1mm×1mm was cut to observe the microstructure. It also shows a good agreement between the simulation and experimental results and the microstructure of 6.5 wt.% Si

steel at the exit of melt-pool was 80 μm equiaxed grain, which was beneficial to improve the quality and properties of the strip.

5 Conclusions

Based on the TSTRC process, a three-dimensional finite element model was established, and the casting process of the 6.5 wt.% Si steel was numerically simulated.

By analyzing the influence of different process parameters on the TSTRC process, it was found that the casting process conditions had a profound impact on TSTRC processing. Simultaneously, it also had an essential impact on the continuity of production and the thin strip's microstructure and quality.

Due to the melt-pool in the TSTRC process, the flow and stirring in the melt-pool were intense, and the turbulence intensity was high. While making the solute distribution in the melt-pool more uniform, it also made the heat exchange effect between the melt and the roll better, accelerated the cooling of the melt, and helped obtain a smaller equiaxed crystal structure. The thin strip structure is closer to the final structure of the finished plate, and the near-final structure of the structure is realized.

The TSTRC experiment was carried out with a pouring temperature of 1457 $^{\circ}\text{C}$, a casting speed of 0.4 m/s, and a melt-pool height of 45 mm. Through the experiment, a high-quality thin strip was obtained. Comparing the microstructure obtained by simulation and experiment, the morphology such as grain size was also consistent with the experimental results. Which not only verifies the correctness of the simulation but also verifies the feasibility of the experiment. Therefore, the TSTRC process can be reasonably predicted by numerical simulation.

Declarations

Authors' contributions Cheng Zhou contributed to the conception of the study; Dongpo Xuan performed the experiment, contributed significantly to analysis and manuscript preparation, performed the data analyses, and wrote the manuscript; Others helped perform the analysis with constructive discussions.

Funding This research did not receive any specific grant from funding agencies in the public, commercial, or not-for-profit sectors.

Data availability The data used to support the findings of this study are included within the article.

Ethics approval and consent to participate Compliance with ethical standards. All authors agreed with the consent to participate.

Consent to publish

That the work described has not been published before (except in the form of an abstract or as part of a published lecture, review, or thesis).

That it is not under consideration for publication elsewhere;

That its publication has been approved by all co-authors, if any;

That its publication has been approved (tacitly or explicitly) by the responsible authorities at the institution where the work is carried out.

Competing interests The authors declare no competing interest.

References

1. Sa GE, Isac M, Guthrie RIL (2013) Progress in strip casting technologies for Steel. *ISIJ Int* 53.(5):729-742. <http://dx.doi.org/10.2355/isijinternational.53.729>
2. Sa GE, Isac M, Guthrie RIL (2012) Progress of strip Casting technology for Steel. *ISIJ Int* 52(12):2109-2122. <http://dx.doi.org/10.2355/isijinternational.52.2109>
3. Spinelli JE, Tosetti JP, Santos CA, Spim JA, Garcia A (2004) Microstructure and solidification thermal parameters in thin strip continuous casting of a stainless steel. *J Mater Process Technol* 150(3):255-262. <http://doi.org/10.1016/j.jmatprotec.2004.02.040>
4. Tavares R, Guthrie R (1998) Computational fluid dynamics applied to twin-roll casting. *Can Metall Quart* 37(3-4):241-250. [https://doi.org/10.1016/S0008-4433\(98\)00011-1](https://doi.org/10.1016/S0008-4433(98)00011-1)
5. Sahoo S, Kumar A, Dhindaw BK, Ghosh S (2012) Modeling and experimental validation of rapid cooling and solidification during high-speed twin-roll strip casting of Al-33 wt pct Cu. *Metall Mater Trans B* 43(4):915-924. <https://doi.org/10.1007/s11663-012-9659-x>
6. Saitoh T, Hojo H, Yaguchi H, Kang CG (1989) Two-dimensional model for twin-roll continuous casting. *Metall Trans B* 20:381-390. <https://doi.org/10.1007/BF02696990>
7. Hwang JD, Lin HJ, Hwang WS, Hu CT (1995) Numerical simulation of metal flow and heat transfer during twin roll strip casting. *ISIJ Int* 35(2):170-177. <http://dx.doi.org/10.2355/isijinternational.35.170>
8. Gupta M, Sahai Y (2000) Mathematical modeling of fluid flow, heat transfer, and solidification in two-roll melt drag thin strip casting of steel. *ISIJ Int* 40(2):144-152. <http://dx.doi.org/10.2355/isijinternational.40.144>
9. Miao YC, Zhang XM, Di HS, Wang GD (2006) Numerical simulation of the fluid flow, heat transfer, and solidification of twin-roll strip casting. *J Mater Process Technol* 174(1-3):7-13. <http://doi.org/10.1016/j.jmatprotec.2005.01.002>
10. Bae JW, Kang CG, Kang SB (2007) Mathematical model for the twin roll type strip continuous casting of magnesium alloy considering thermal flow phenomena. *J Mater Process Technol* 191(1-3):251-255. <http://doi.org/10.1016/j.jmatprotec.2007.03.058>
11. Pei ZP, Ju DY, Li X (2017) Simulation of critical cooling rate and process conditions for metallic glasses in vertical type twin-roll casting. *T Nonferr Metal Soc* 27(11):2406-2414.

[https://doi.org/10.1016/S1003-6326\(17\)60267-X](https://doi.org/10.1016/S1003-6326(17)60267-X)

12. He C, Yu W, Li Y, Wang Z, Wu D, Xu G (2020) Relationship between cooling rate, microstructure evolution, and performance improvement of an Al–Cu alloy prepared using different methods. *Mater Res Express* 7(11):116501-116515. <http://doi.org/10.1088/2053-1591/abc4f9>
13. Zeng J, Koitzsch R, Pfeifer H, Friedrich B (2009) Numerical simulation of the twin-roll casting process of magnesium alloy strip. *J Mater Process Technol* 209(5):2321-2328. <http://doi.org/10.1016/j.jmatprotec.2008.05.032>
14. Li JT, Xu GM, Yu HL, et al. (2015) Optimization of process parameters in twin-roll strip casting of an AZ61 alloy by experiments and simulations. *Int J Adv Manuf Technol* 76(9-12):1769-1781. <http://doi.org/10.1007/s00170-014-6312-7>
15. Guan RG, Zhao ZY, Zhang Q (2013) Effect of the casting temperature on temperature field and microstructure of A2017 alloy during an innovative continuous semisolid rolling process with a vibrating sloping plate device. *Int J Adv Manuf Technol* 67(1-4):917-923. <http://doi.org/10.1007/s00170-012-4536-y>
16. Sun M, Zhu Z, Zheng L, Guo S, Du F (2020) Study on the influence of vibration parameters in the twin-roll strip vibration cast-rolling process. *Int J Adv Manuf Technol* 108(4):3141–3157. <https://doi.org/10.1007/s00170-020-05432-5>
17. Hu Z, Li P, He L (2011) Coupled analysis of temperature and flow during twin-roll casting of magnesium alloy strip. *J Mater Process Technol* 211(6):1197-1202. <https://doi.org/10.1016/j.jmatprotec.2011.02.001>
18. Rodrigues C, Ludwig A, Wu M, Kharicha A, Vakhrushev A (2020) Two-phase viscoplastic model for the simulation of twin roll casting. *J Mater Process Technol* 286:116814. <https://doi.org/10.1016/j.jmatprotec.2020.116814>
19. Wang D, Zhou C (2014) A top side-pouring twin-roll caster for metals strips. *J Mater Process Technol* 214(4):916–924. <https://doi.org/10.1016/j.jmatprotec.2013.12.001>
20. Zhang HZ, Zhou C, Wei CX (2017) Mathematical and physical modeling of metal delivery system during top side-pouring twin-roll casting. *J Mater Process Technol* 254:1-12. <https://doi.org/10.1016/j.jmatprotec.2017.11.016>
21. Wang D, Zhou C, Xu GJ, Huaiyuan A (2014) Heat transfer behavior of top side-pouring twin-roll casting. *J Mater Process Technol* 214(6):1275–1284. <https://doi.org/10.1016/j.jmatprotec.2014.01.009>
22. Zhang HZ, Zhou C, Wei CX (2017) Numerical Simulation of thermal field of work roll during top side-pouring twin-roll casting of steel. *ISIJ Int.*57(10):1811-1820. <http://dx.doi.org/10.2355/isijinternational.ISIJINT-2017-191>
23. Barekar NS, Dhindaw BK (2014) Twin-roll casting of aluminum alloys. *Mater Manuf Process* 29(6):651-661. <http://dx.doi.org/10.1080/10426914.2014.912307>

24. Fan Z, Liu G (2005) Solidification behaviour of AZ91D alloy under intensive forced convection in the RDC process. *Acta Mater* 53(16):4345-4357. <https://doi.org/10.1016/j.actamat.2005.05.033>
25. Kim WS, Kim DS, Kuznetsov AV (2000) Simulation of coupled turbulent flow and heat transfer in the wedge-shaped pool of a twin-roll strip casting process. *Int J Heat Mass Tran* 43(20):3811-3822. [https://doi.org/10.1016/S0017-9310\(00\)00013-2](https://doi.org/10.1016/S0017-9310(00)00013-2)
26. Zhang XM, Jiang ZY, Yang LM, Liu XH, Wang GD, Tieu AK (2007) Modelling of coupling flow and temperature fields in molten pool during twin-roll strip casting process. *J Mater Process Technol* 187:339-343. <https://doi.org/10.1016/j.jmatprotec.2006.11.064>
27. Liu H, Liu Z, Li C, Cao G, Wang G (2011) Solidification structure and crystallographic texture of strip casting 3 wt.% Si non-oriented silicon steel. *Mater Charact* 62(5):463-468. <https://doi.org/10.1016/j.matchar.2011.02.010>
28. Pirhayati P, Aval HJ (2019) An investigation on thermo-mechanical and microstructural issues in friction surfacing of Al-Cu aluminum alloys. *Mater Res Express* 6(5). <https://orcid.org/0000-0002-5431-0413>
29. Wei C, Li S (2011) Effect of temperature gradient on grain growth behavior from phase field simulations. *Acta Phys Sin* 60(10):132-139. <https://doi.org/10.7498/aps.60.100701>
30. Lee YS, Kim HW, Cho JH (2015) Process parameters and roll separation force in horizontal twin roll casting of aluminum alloys. *J Mater Process Technol* 218:48-56. <https://doi.org/10.1016/j.jmatprotec.2014.11.031>
31. Santos CA, Quaresma J, Garcia A (2001) Determination of transient interfacial heat transfer coefficients in chill mold castings. *J Alloy Compd* 319(1-2):174-186. [https://doi.org/10.1016/S0925-8388\(01\)00904-5](https://doi.org/10.1016/S0925-8388(01)00904-5)
32. Hyndman RJ, Koehler AB (2006) Another look at measures of forecast accuracy. *Int J Forecasting*. 22(4):679-688 <https://doi.org/10.1016/j.ijforecast.2006.03.001>

Figures

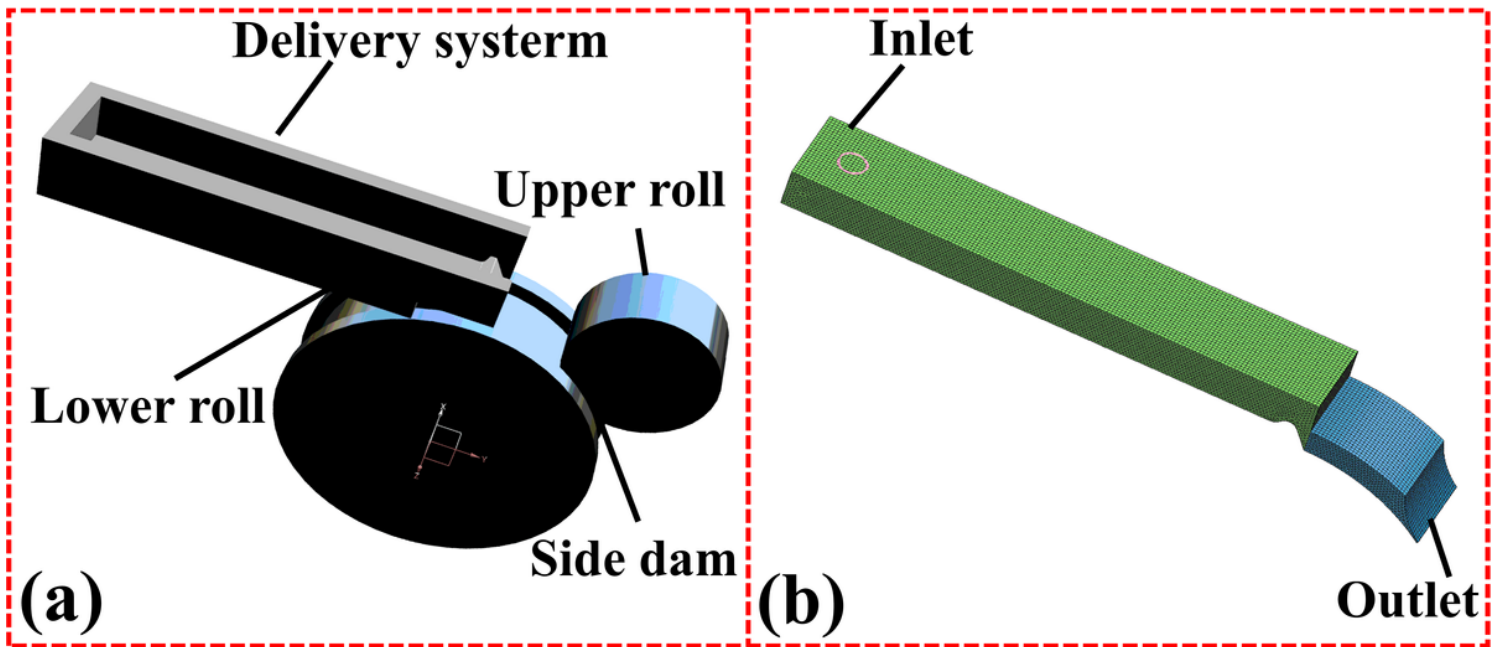


Figure 1

The three-dimensional schematic model a and simulation area b of the TSTRC process

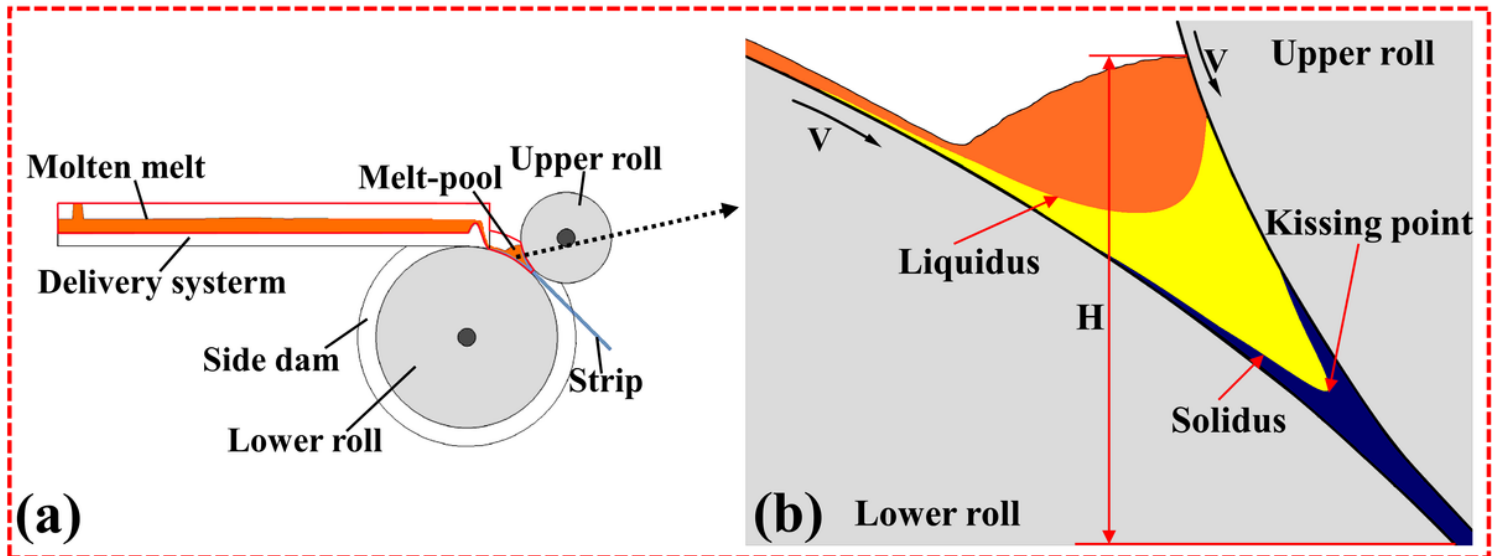


Figure 2

The schematic diagram of the TSTRC process a and enlarged view of the melt-pool b

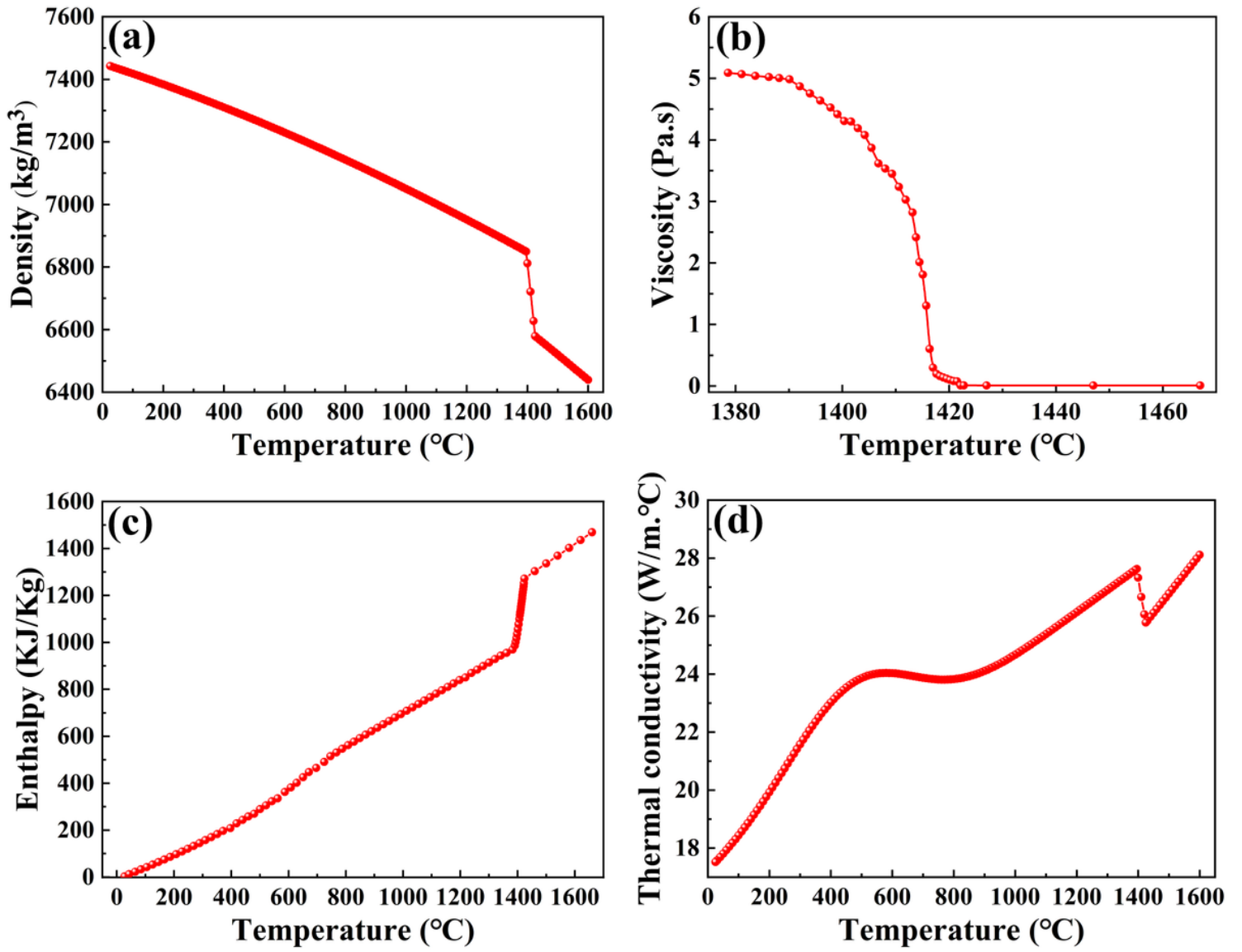


Figure 3

Thermal properties of 6.5 wt.% Si steel: a density, b viscosity, c enthalpy, and d thermal conductivity

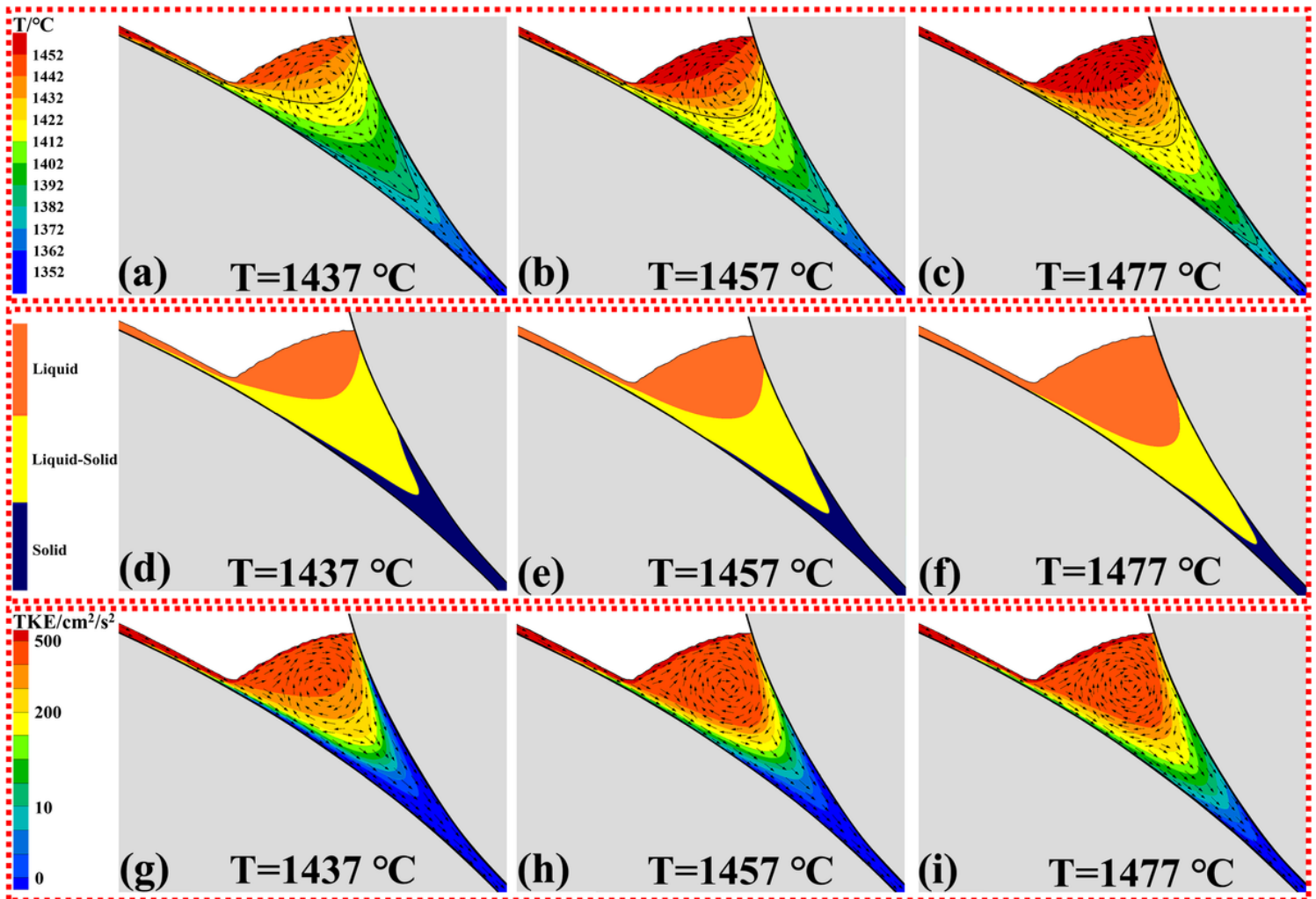


Figure 4

The temperature field and flow field a-c, solidification field d-f, turbulent energy, and flow field g-i in melt-pool at different pouring temperatures

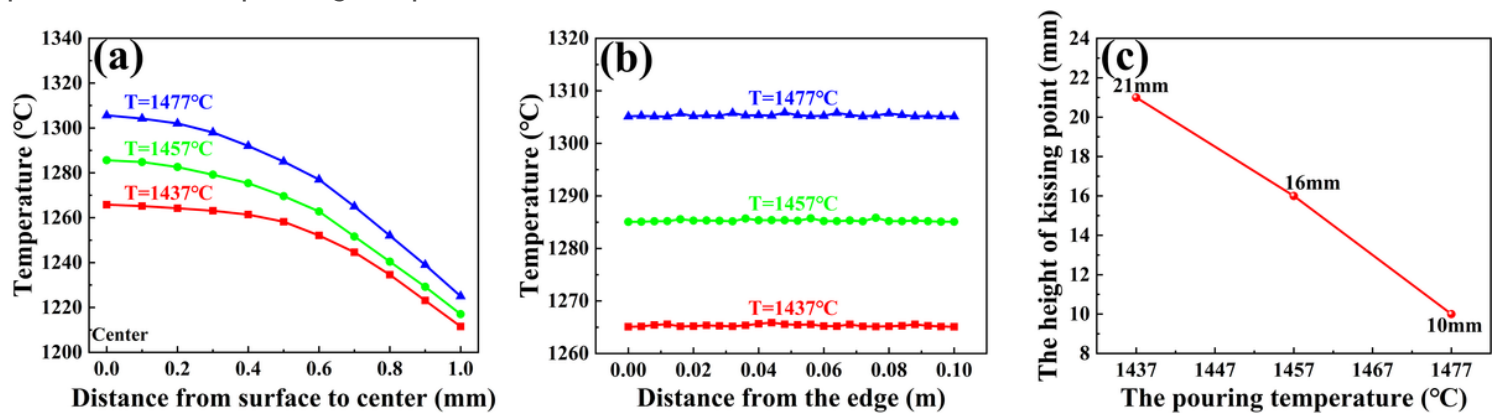


Figure 5

Under different pouring temperatures: a the temperature of the melt-pool outlet, b the temperature of the centerline of the melt-pool outlet, c the height of the kissing point

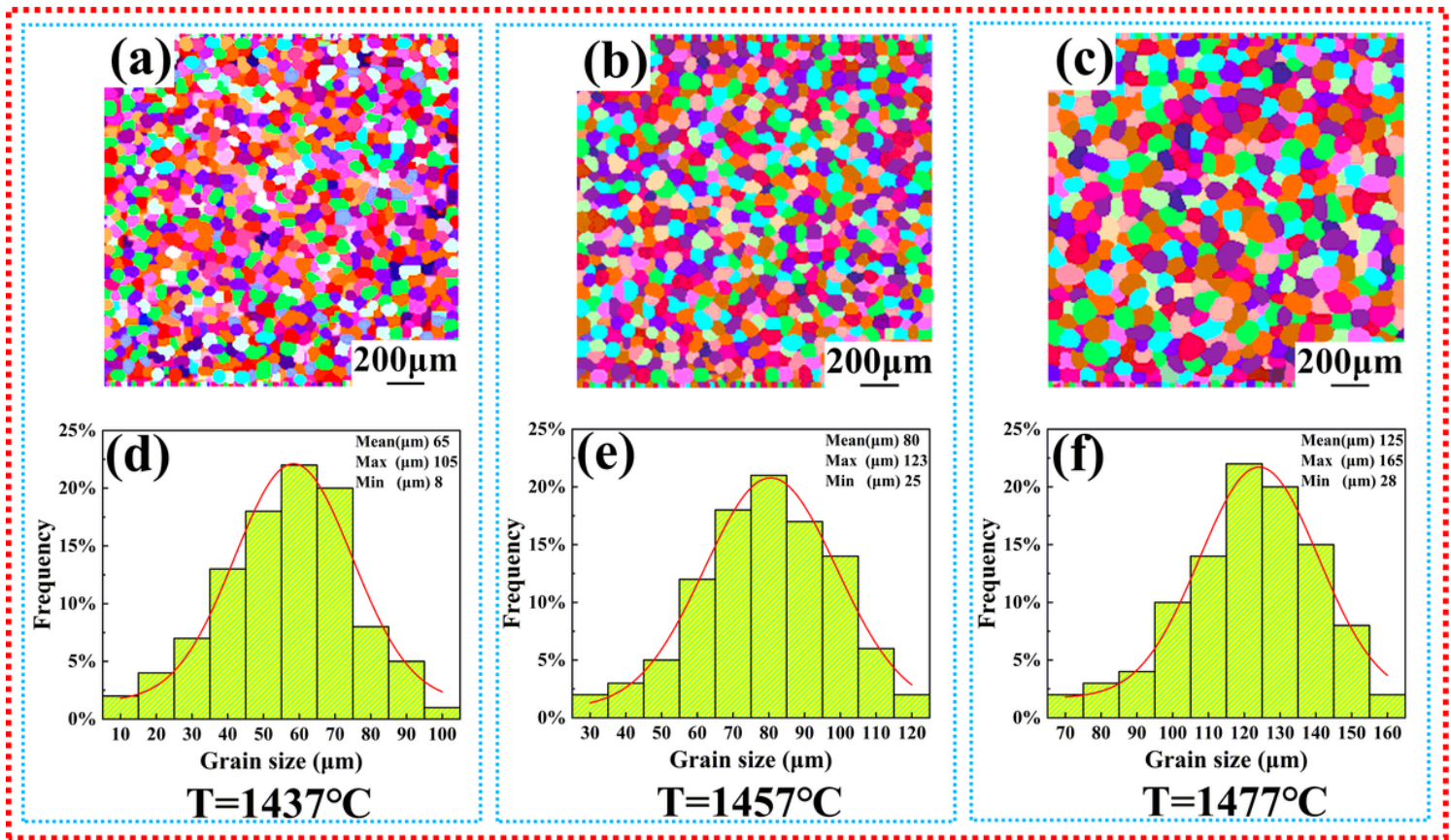


Figure 6

The microstructure a-c and the grain size d-f at different pouring temperatures

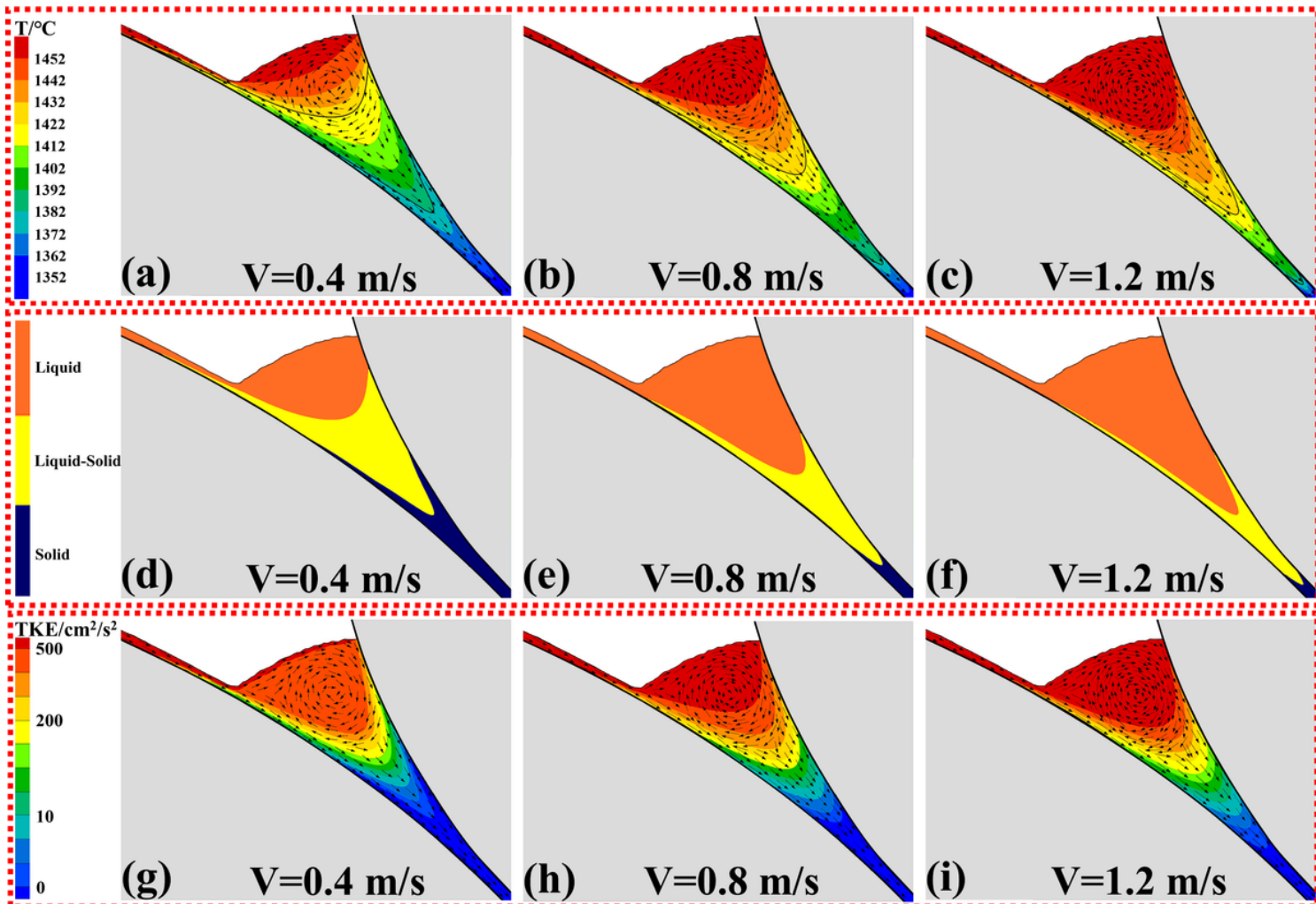


Figure 7

The temperature field and flow field a-c, solidification field d-f, turbulent energy, and flow field g-i in melt-pool at different casting speeds

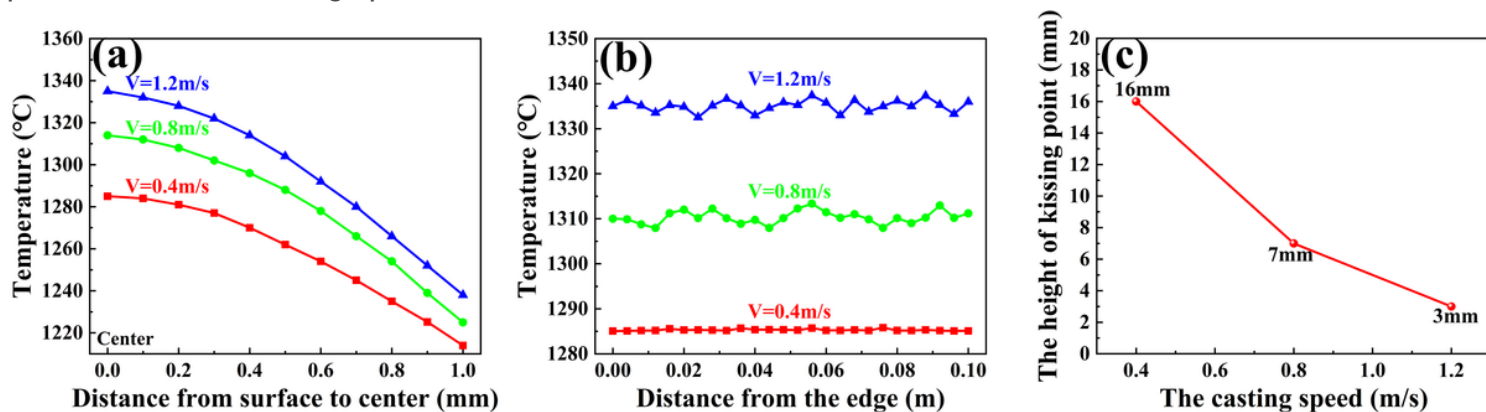


Figure 8

At different casting speeds: a the temperature of the melt-pool outlet, b the temperature of the centerline of the melt-pool outlet, c the height of the kissing point

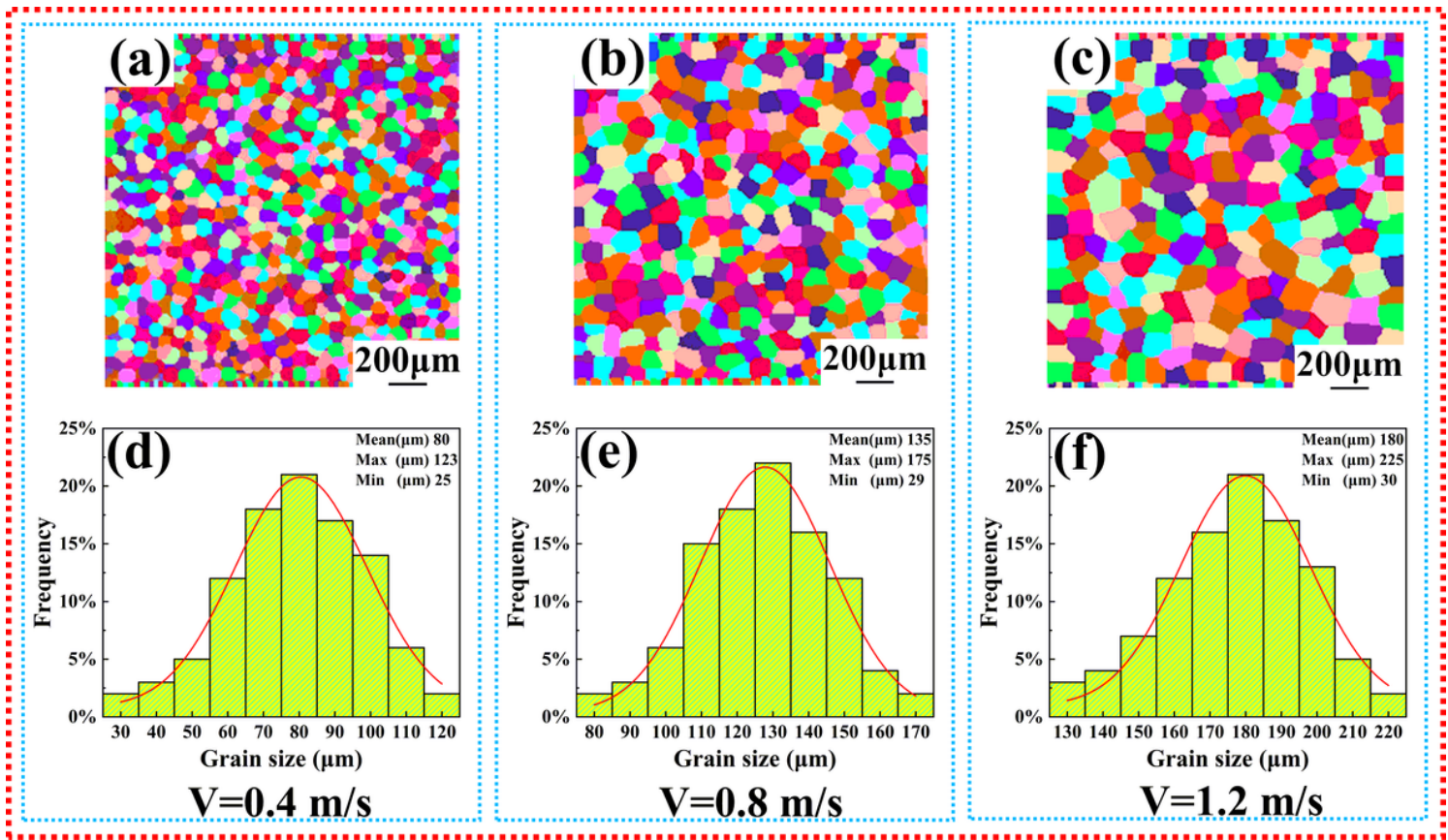


Figure 9

The microstructure a-c and the grain size d-f at different casting speeds

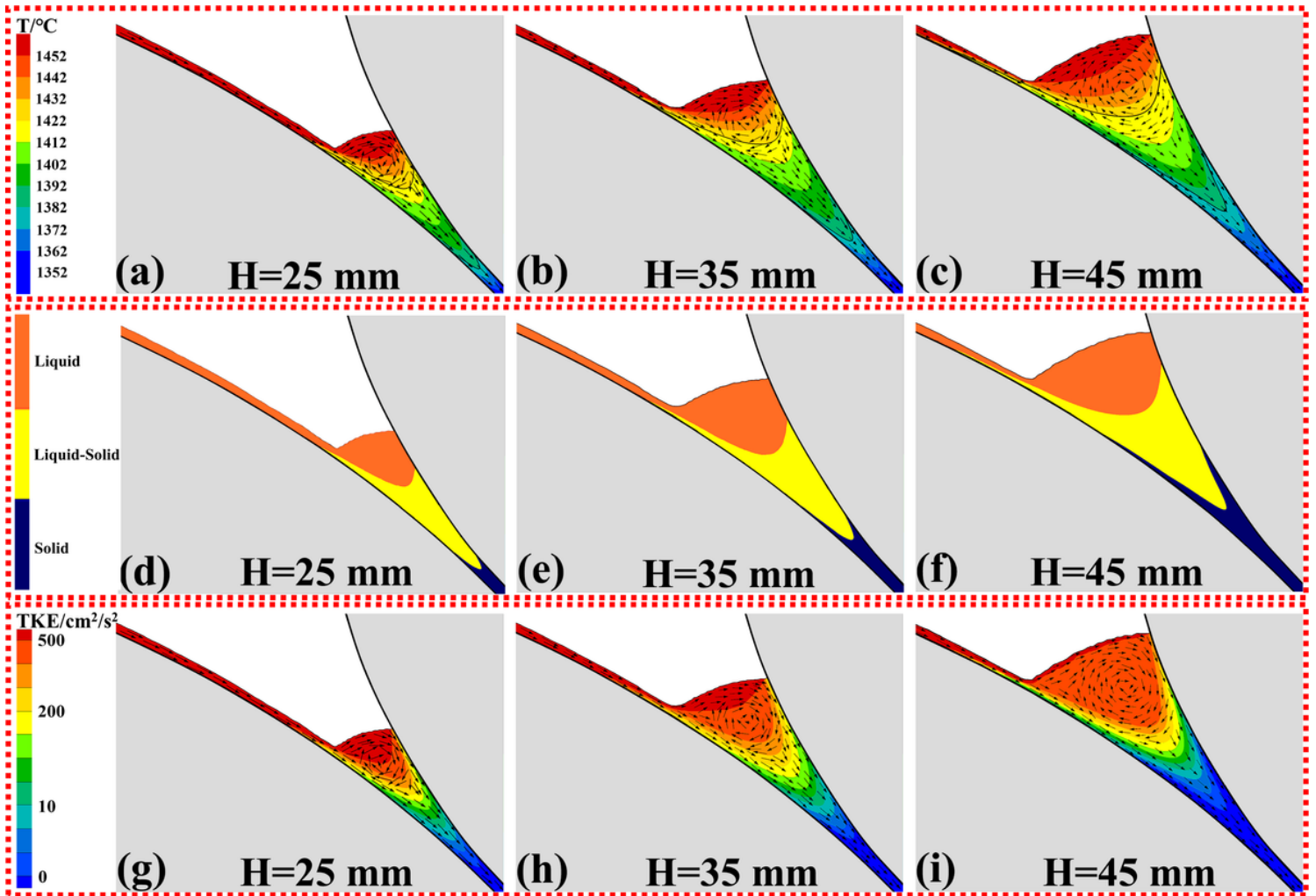


Figure 10

The temperature field and flow field a-c, solidification field d-f, turbulent energy, and flow field g-i in melt-pool at different melt-pool heights

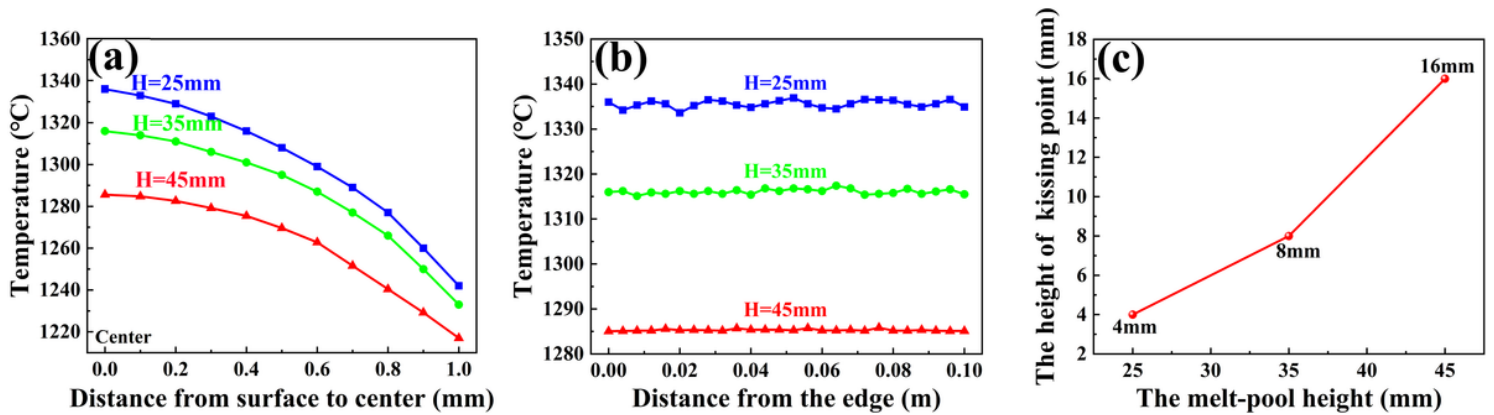


Figure 11

Under different melt-pool heights: a the temperature of the melt-pool outlet, b the temperature of the centerline of the melt-pool outlet, c the height of the kissing point

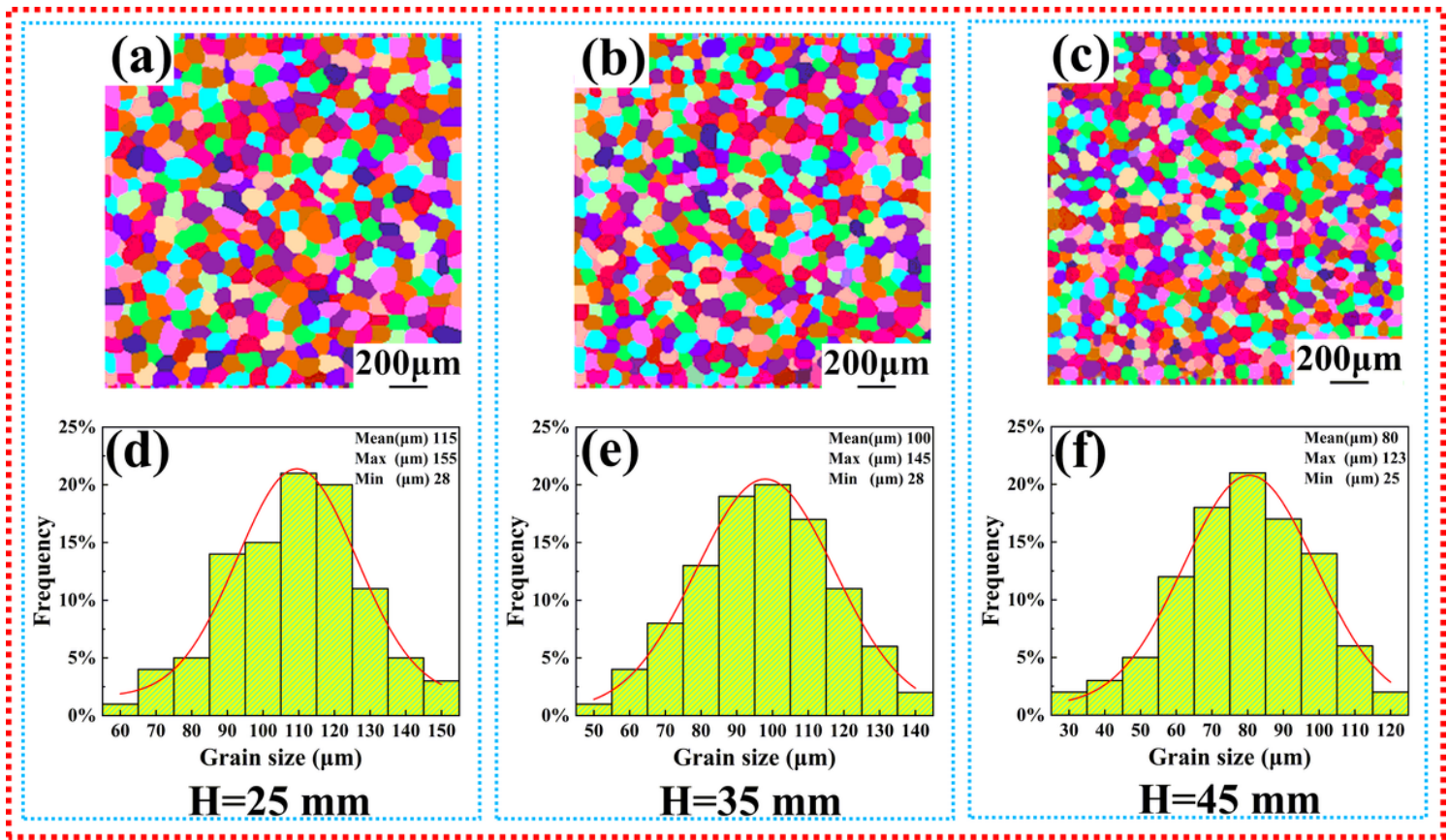


Figure 12

The microstructure a-c and the grain size d-f at different melt-pool heights

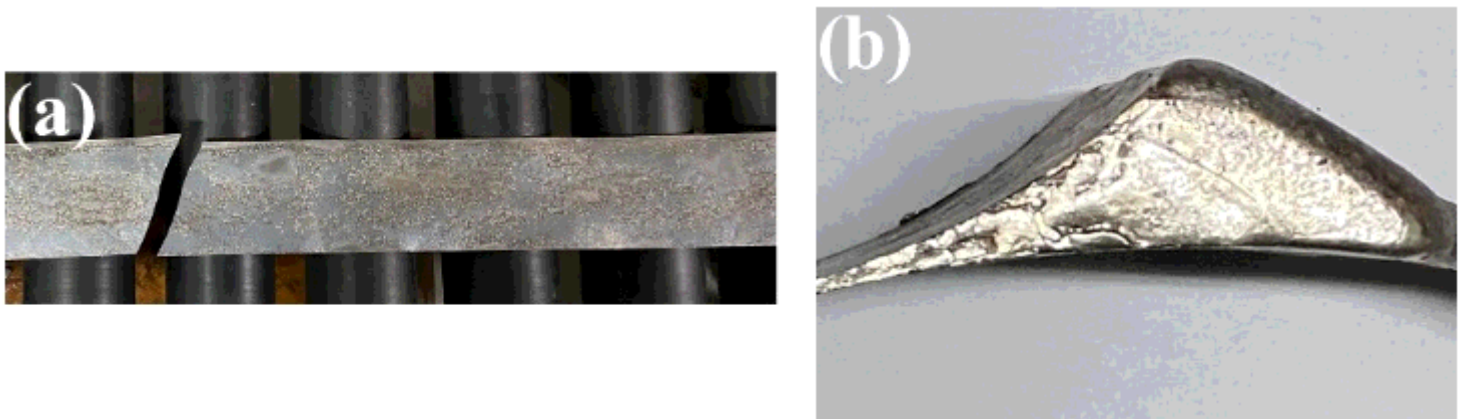


Figure 13

Thin strip fracture photo a and stuck sample b

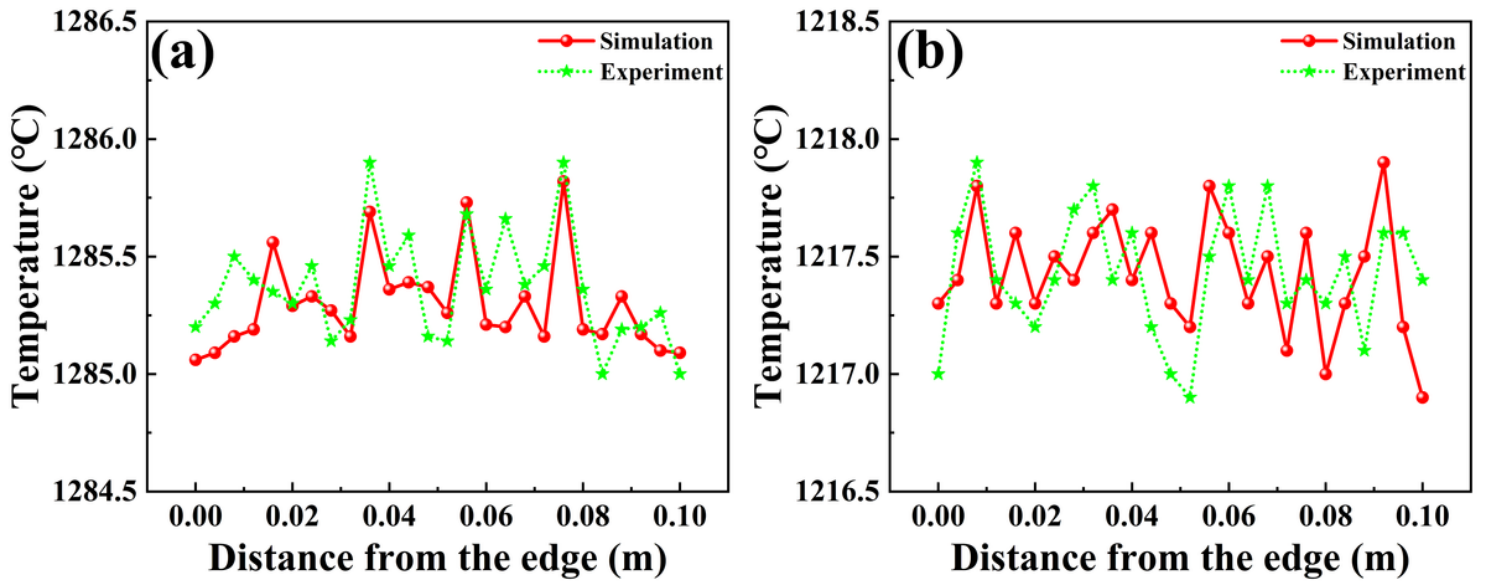


Figure 14

The simulation results and experimental results of the outlet temperature of the melt-pool: a the temperature of the centerline of the melt-pool outlet; b the surface temperature of the melt-pool outlet

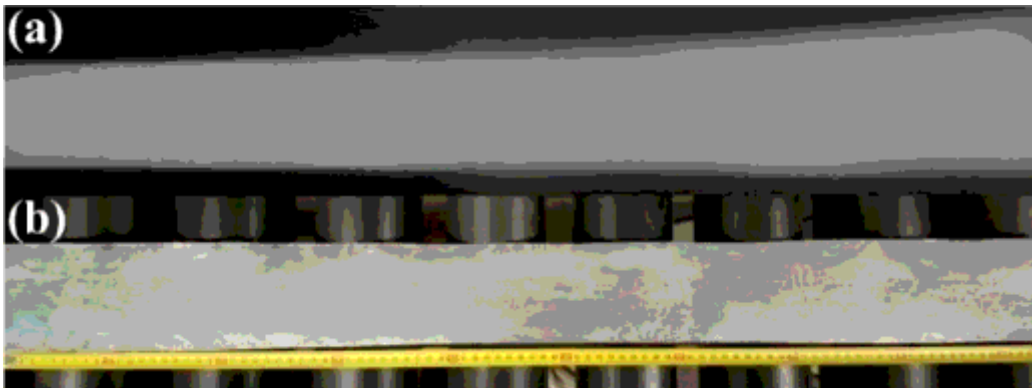


Figure 15

The 6.5 wt.% Si steel strip produced by TSTRC

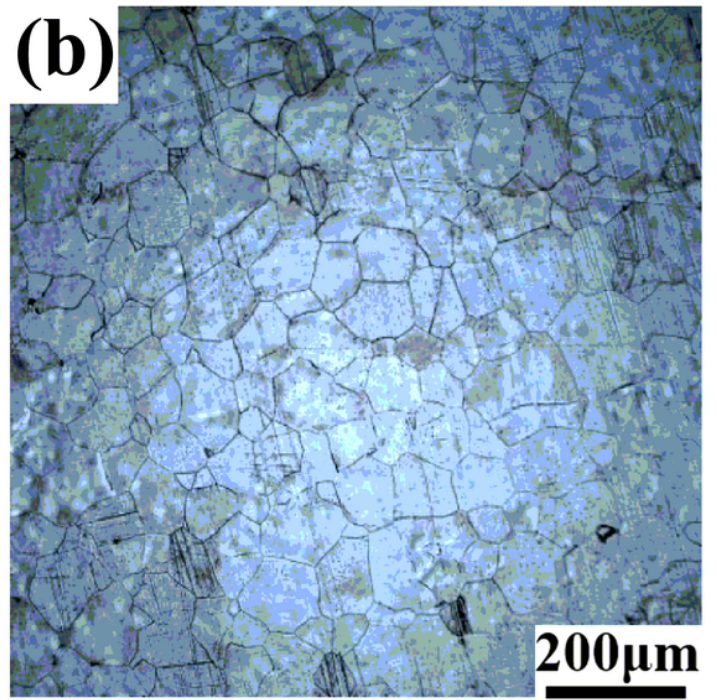
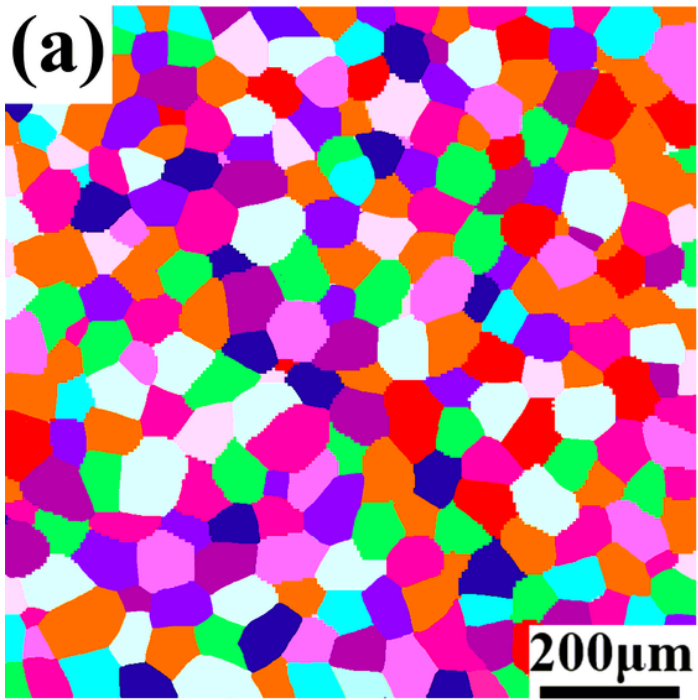


Figure 16

The microstructure by simulation and experiment at the exit of the melt-pool